

The Deutsch Field Gamma-Ray Pulsar Paper I : The Model Basics

M.G. Higgins & R.N. Henriksen

Queen's University, Kingston, Ontario, Canada

Submitted 1996 January 25

ABSTRACT

A new model for the high-energy emission from pulsars is developed by considering charged particle motion in the fields of a spinning, highly magnetised and conducting sphere in vacuum. A generally applicable approximation to the particle motion in strong fields is developed and applied to the numerical modelling, and the radiation emitted by curvature emission is summed to generate light curves. The model predicts many of the observed features of pulsar light curves. This paper outlines the basic properties of the model; a subsequent paper will discuss the statistical properties of a population of model pulsars and apply the model to the known gamma-ray pulsars.

Key words: pulsars — gamma rays — Deutsch fields — electron acceleration.

1 INTRODUCTION

Much work has been done over the past twenty-five years on the low-frequency radio emission detected from pulsars, in large part due to the huge volume of data available. In the last decade, however, attention has been turning toward the high end of the emission spectrum, as more reliable data become available (see, for example, Grenier et al 1993 and Masnou et al 1994).

The main problem in developing a theoretical model of the pulsar magnetosphere is the complexity of finding a self-consistent solution to the set of equations defining the electromagnetic fields and particle densities and velocities as functions of time. Theoretical attempts to model the high-energy emission generally make assumptions about the global structure of the magnetosphere, and then restrict their attention to local sites where large electric fields parallel to the magnetic field lines accelerate charges. The two most developed examples are the polar cap model of Daugherty & Harding (1994) and the outer gap model created by Cheng, Ho, & Ruderman (1986) and further developed by Chiang & Romani (1994).

We make a set of assumptions about the global magnetospheric structure that differs from past models: we assume that the charge density is very small in the outer magnetosphere, and that the pulsar can be treated as a spinning, highly magnetised and conducting sphere in vacuum (the electromagnetic fields around such a star were derived by Deutsch 1955). This assumption is justified in our model because we find that any charges created in the inner magnetosphere follow paths constrained to stay close to the star. They are thus unable to populate the outer magnetosphere

and short out the electric fields (the distinction between the inner and outer magnetosphere is elaborated in section 3.2).

By so fixing the fields, particle motion can be integrated relatively easily, and the radiation observed from the model pulsar can be estimated fairly accurately. With low number densities, inverse Compton scattering and photon/photon interactions are unlikely, and synchrotron emission is not important, so curvature radiation is the only source of emission. The back reaction on the particles of the curvature emission is included in the determining the particle energies.

An approximation to the particle motion in strong fields is developed which is applicable in all realistic pulsar magnetospheres where gamma-ray production is efficient. The approximation is used to simplify our numerical integration, but is general enough that it may find application in other models of the pulsar magnetosphere.

In this paper (Paper I), the basic characteristics of the model will be examined. Higgins & Henriksen (1996) (hereafter Paper II) will apply the model to the known high-energy pulsars, consider how the model pulsar ages, and estimate the number of high-energy pulsars that should be found in gamma-ray surveys.

2 THE DEUTSCH FIELDS AND THE VACUUM APPROXIMATION

2.1 The Deutsch Fields

By fixing the electromagnetic fields, the problem of calculating the radiation pattern changes from a system of par-

arXiv:astro-ph/9601157v1 26 Jan 1996

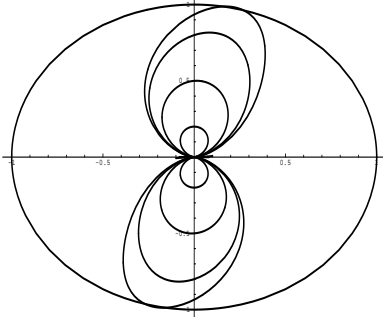


Figure 1. Selected closed field lines for the orthogonal Deutsch field pulsar in the plane perpendicular to the rotation axis. The circle shows the light cylinder, and the dimensions are in units of the light cylinder radius R_{lc} .

tial differential equations to a system of ordinary differential equations, and becomes much more tractable.

The Deutsch fields look like the fields of a spinning magnetic point dipole at radii much larger than the stellar radius, with wrapped-up magnetic field lines outside the light cylinder and large components of electric field parallel to the magnetic field. Inside the star the electric field is frozen-in, and this boundary condition at the stellar surface significantly perturbs the fields near the star. Field lines in the plane perpendicular to the rotation axis for the orthogonal Deutsch fields (when the magnetic dipole moment is perpendicular to the rotation axis) near the light cylinder are shown in Figure 1 for selected closed field lines and Figure 2 for open field lines.

Four parameters entirely characterise these fields: the angular velocity of the star Ω , the radius of the star a , the magnitude of the effective magnetic dipole moment μ , and the inclination χ of the dipole moment with respect to the rotation axis.

An estimate of the electric and magnetic field strength is useful for the calculation of various quantities; the order of magnitude of the electric and magnetic fields near the light cylinder is approximately

$$E \simeq B \simeq \frac{\mu\Omega^3}{c^3} \quad (1)$$

The vacuum approximation holds as long as the charge densities and current densities give negligible perturbations to the fields. This is true when the charge density is much less than the Goldreich-Julian charge density:

$$\rho_{GJ} \simeq \frac{\vec{\Omega} \cdot \vec{B}}{2\pi c} \quad (2)$$

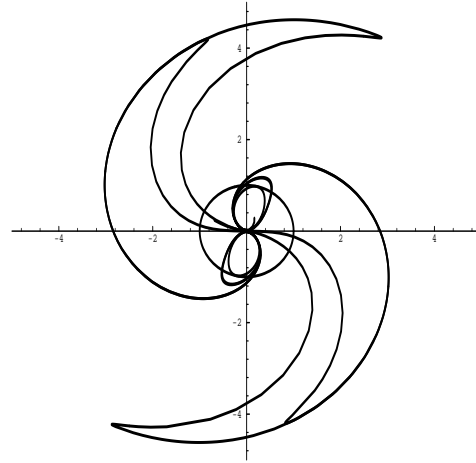


Figure 2. Selected open field lines for the orthogonal Deutsch field pulsar in the plane perpendicular to the rotation axis. The circle shows the light cylinder, and the dimensions are in units of the light cylinder radius R_{lc} .

where the fields are frozen-in. Here, $\vec{\Omega}$ is the angular velocity of the star and \vec{B} is the magnetic field at the point in question. This corresponds approximately to a number density:

$$n_{GJ} \simeq 4 \times 10^4 \text{ cm}^{-3} \left(\frac{\Omega}{100 \text{ rads/s}}\right)^4 \left(\frac{\mu}{10^{30} \text{ G-cm}^3}\right) \left(\frac{R_{lc}}{r}\right)^3 \quad (3)$$

where $R_{lc} = c/\Omega$ is the radius of the light cylinder. Note the strong variation with the angular velocity of the star; a relatively small charge density at the light cylinder of a slow pulsar can alter the fields.

The fields far from the star look like a spherically-propagating electromagnetic wave with frequency equal to the rotational frequency of the star. This radiation removes rotational energy from the star, slowing it with time. Therefore, the effective magnetic dipole moment of the Deutsch fields can be estimated from the period and period derivative of the pulsar rotation:

$$\mu \simeq 3.2 \times 10^{37} (P\dot{P})^{1/2} \frac{\left(\frac{I}{10^{45} \text{ g-cm}^2}\right)^{1/2}}{\sin \chi} \quad (4)$$

The moment of inertia of neutron stars is unknown by up to a factor of 10 depending on the equation of state;

this introduces some uncertainty into the calculation of the effective magnetic dipole moment.

This result is similar to that of magnetodipole radiation from a point dipole derived by Ostriker & Gunn (1969), since the Deutsch fields only differ from the point dipole fields near the star.

2.2 Particle-Photon and Photon-Photon Interactions

This model assumes that the only emission contributing to the light curves is a result of curvature radiation by the high-energy particles moving along curved paths in the magnetosphere. This is justified as long as the number densities are small; how small can be roughly calculated by examining the mean free path of photons subject to Compton scattering off electrons and to self-scattering.

2.2.1 Inverse Compton Scattering

The cross-section for Compton scattering (or inverse Compton scattering) is approximately equal to the Thompson scattering cross-section for photon energies in the electron rest frame much less than the electron rest mass. For photon energies in this frame much greater than the electron rest mass, the cross-section is approximately $\frac{3}{4}\sigma_{\text{T}}mc^2/E_{\gamma}$ (Jackson 1975). Therefore, the Thompson cross-section will be used as an upper limit to the cross-section (although this neglects resonant interactions with the magnetic field, which can increase the cross-section by several orders of magnitude above the Thompson value for a limited energy range - see, for example, Daugherty & Harding 1991).

The optical depth of the magnetosphere to inverse Compton scattering for a photon is then approximately

$$\tau_{\text{ICS}} \simeq n_e \sigma_{\text{T}} R_{\text{lc}}$$

where n_e is an average electron density, $\sigma_{\text{T}} = 6.65 \times 10^{-25} \text{ cm}^2$ is the Thompson scattering cross-section, and $R_{\text{lc}} = c/\Omega$ is the light cylinder radius.

The number density of photons in the magnetosphere can be roughly estimated from the power output of each electron P_e , the average photon energy E_{γ} , and the characteristic time the photons are within the magnetosphere $1/\Omega$ as

$$n_{\gamma} \simeq \frac{P_e}{\Omega E_{\gamma}} n_e \quad (5)$$

To ensure that the number of photons which scatter off electrons is much less than the number of electrons,

$$n_{\gamma} \tau_{\text{ICS}} \ll n_e$$

This puts a limit on the number density of electrons of

$$n_e \ll \frac{\Omega^2 E_{\gamma}}{\sigma_{\text{T}} c P_e} \quad (6)$$

For relativistic motion on a path with radius of curvature ρ , the power and average frequency of curvature emission can be written (e.g., Jackson 1975)

$$P_e = \frac{2}{3} \frac{e^2 c}{\rho^2} \gamma^4 \quad (7)$$

$$E_{\gamma} \simeq \hbar \frac{c}{\rho} \gamma^3 \quad (8)$$

where γ is the charge's Lorentz factor and e its charge.

Substituting these into inequality (6),

$$n_e \ll \frac{\hbar \Omega}{\sigma_{\text{T}} e^2 \gamma} \quad (9)$$

The Lorentz factor of particles can be estimated from the fields (see equation (14)) by equating the power output from radiation with the power input from the electric field. Roughly, this gives

$$\gamma^4 \simeq \frac{\Omega \mu}{ec}$$

This can be used to define an upper limit to a combination of the stellar parameters below which this model remains applicable by setting the Golreich-Julian number density equal to the limit of equation (9) (the number densities must always be much less than the Golreich-Julian number density). Using the expression for γ above, the condition for negligible scattering is

$$\Omega^{\frac{13}{4}} \mu^{\frac{5}{4}} \ll 3.3 \times 10^{49} \quad (10)$$

For example, with a magnetic dipole moment of 10^{30} G cm^3 (giving a surface magnetic field of approximately 10^{12} G), the upper limit on Ω is approximately 5000 rad/s, much larger than any standard pulsar spin rates. Thus, for the population of normal pulsars, the Goldreich-Julian number density is not sufficient to ensure significant Compton scattering.

2.2.2 Photon-Photon Scattering

A similar calculation can be done for the case of photon-photon scattering, where the cross-section above the pair production limit is again maximally of order the Thompson cross-section. For the spectrum to remain unperturbed as it leaves the magnetosphere,

$$\tau_{\gamma-\gamma} \ll 1$$

where $\tau_{\gamma-\gamma} = n_{\text{photon}} \sigma_{\text{T}} R_{\text{lc}}$. This gives exactly the same constraint on the electron number density and on the angular velocity and dipole moment (equation (10)) as the inverse Compton scattering criterion above.

While the fraction of photons affected by photon-photon scattering is rather small, the photons which do interact create charges in the magnetosphere. This could provide a source for the charges, though a more complex calculation is required to properly examine the viability of this option.

2.3 Synchrotron Radiation

A key approximation of the model (see section 3.1) is that charges move parallel to the magnetic field line in a frame where the electric and magnetic fields are parallel. Therefore, in the framework of the model, there is no contribution at all from synchrotron radiation. The results of simulating particle motion under this approximation have been compared to those found in a full-blown simulation of the particle motion where the approximation is relaxed. The two calculations agree remarkably well whenever the fields and

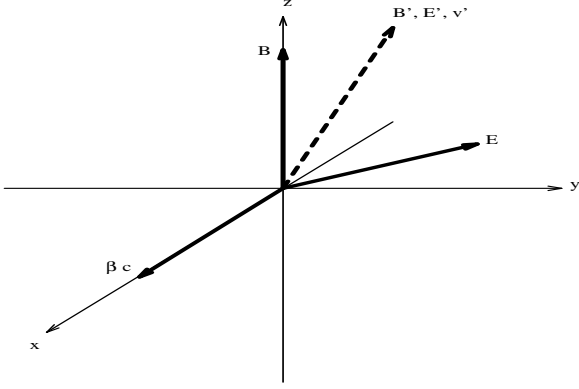


Figure 3. A boost along the x -axis shown in the figure moves into a frame where the electric field \vec{E}' is parallel to the magnetic field \vec{B}' . In the pulsar rest frame, the z -axis is taken to be parallel to \vec{B} , and \vec{E} lies in the y - z plane. In the boosted frame, the charges are assumed to move either parallel or anti-parallel to \vec{B}' .

energies are large enough to produce significant amounts of radiation.

3 PARTICLE MOTION AND EMISSION

3.1 The Drift Frame Bead-on-a-Wire Approximation of Particle Motion

The numerical integration of the charged particle motion in the simulations is simplified enormously under the application of a key assumption in this work, labelled the drift frame bead-on-a-wire (DFB) approximation. We assume that, in a frame where the electric field is parallel to the magnetic field, the charge has a velocity directed parallel or antiparallel to \vec{B} with magnitude approximately equal to c ; the velocity in the pulsar rest frame at any point can then be determined by boosting back to the original frame of reference.

Consider a point in the magnetosphere with electric field \vec{E} and magnetic field \vec{B} . Define the z -axis to be parallel to \vec{B} , and \vec{E} to have components only in the z and y directions. There is a boost of $v = c\beta\hat{x}$ which defines a frame of reference where \vec{E}' is parallel to \vec{B}' as long as the electric field is not perpendicular to the magnetic field *and* equal in magnitude (primed quantities are those in the boosted frame). This is shown in Figure 3; the boost can be shown to be

$$\beta = \frac{B^2 + E^2 - \sqrt{(B^2 + E^2)^2 - 4B^2 E_y^2}}{2BE_y} \quad (11)$$

where all the quantities relate to the pulsar rest frame. This is valid for $E > B$ or $E < B$, and even $E = B$ as long as the two are not perpendicular.

We assume that, in this frame, the velocity of the charge is either parallel or anti-parallel to \vec{B}' (depending on the sign of $q\vec{E} \cdot \vec{B}$, where q is the particle's charge) and that the particle is ultra-relativistic, so its speed is nearly c . Boosting back to the initial frame, the charge's velocity is then

$$\vec{v} = c\beta\hat{x} \pm \frac{c}{\gamma} \frac{B'_y}{B'} \hat{y} \pm \frac{c}{\gamma} \frac{B'_z}{B'} \hat{z} \quad (12)$$

$$= c\beta\hat{x} \pm \frac{c}{\gamma} \frac{\beta E_z}{U} \hat{y} \pm \frac{c}{\gamma} \frac{B - \beta E_y}{U} \hat{z} \quad (13)$$

where $U = \sqrt{B^2 + \beta^2 E^2 - 2\beta E_y B}$ and $\gamma = 1/\sqrt{1 - \beta^2}$. The expression is exact, given the assumption about the particle motion in the boosted frame of reference.

Given an initial position, the charge's motion is now defined by the solution to a set of three first-order ordinary differential equations $\vec{v} = d\vec{r}/dt$, which can be solved numerically with relative ease. The particle's energy can be found by integrating the power input due to the electric field and the power output due to the radiation loss. The simulations of particle motion under this approximation have been compared to those when the DFB approximation is relaxed in a more sophisticated (and time-consuming) simulation and are found to match very closely for all the known gamma-ray pulsars (the constraint on the applicability of the DFB approximation is considered below).

It is generally found that, since the fields are so large, the radiation reaction force acts like a thermostat, balancing the energy input from the electric force with the energy output due to radiation. This gives a convenient description of the particle's energy at any point,

$$\gamma^4 = \frac{3}{2} \frac{q\vec{E} \cdot \vec{v}\rho^2}{e^2 c} \quad (14)$$

where the radiative power output was taken as equation (7).

The whole approximation is only valid where the timescale to radiate away the momentum perpendicular to the field direction is much less than the timescale $1/\Omega$ over which the fields vary significantly; this reduces to another constraint on Ω and μ :

$$\Omega^{\frac{21}{4}} \mu^{\frac{9}{4}} \gg 5 \times 10^{71} \quad (15)$$

For a typical $\mu = 10^{30} \text{ G cm}^3$, this gives $\Omega \gg 6 \text{ rad/s}$, which is true for all the observed gamma-ray pulsars.

3.2 Types of Particle Motion and Justification of the Vacuum Assumption

Three different types of particle motion were observed in the simulations. Some charges follow open paths and escape to infinity, radiating quite powerfully inside the magnetosphere; these are labelled "outgoing" paths. The second and third types of path are closed within the inner magnetosphere. Charges on the second type of path follow a course which directs them into the star; on the third variety, the charge paths attempt to cross a surface where $\vec{E} \cdot \vec{B}$ goes to zero. Particles encountering such a "null surface" lose their energy almost immediately since the radiation power output is no longer balanced by an energy input from the electric field. Any charge encountering a null surface is forced to remain on it; the electric field switches sign on either side of the surface, effectively trapping the particle. They can travel out of the magnetosphere on these surfaces at relatively low energies without contributing to the observed radiation, but perhaps establishing the required charge balance for the steady-state magnetosphere. These surfaces then are not so much "gaps" as "conduits" for low-energy plasma.

Which type of path a charge will follow depends on its starting position. The fraction of paths which are outgoing drops to zero at a radius of approximately $0.1R_{lc}$; all the

charges inside this radius are bound to the inner magnetosphere, except those on the surface with $\vec{E} \cdot \vec{B} = 0$, which can escape the magnetosphere but at very low energies. This defines the boundary between the inner and outer magnetosphere: inside the inner magnetosphere, all particle paths are bound.

This constitutes our justification of the evacuated nature of the magnetosphere; charges created (presumably due to $\gamma - B$ pair creation near the star) will not be able to populate the outer magnetosphere, since they are locked into bound orbits. We take the bound charges into account by increasing the effective stellar radius to $0.1R_{\text{lc}}$. In doing so, the charges remain bound, even though the field structure changes to become “frozen-in”.

When charges are started relatively far inside the magnetosphere, but outside $0.1R_{\text{lc}}$, most of the paths are still bound, and the outgoing paths extend from a small region near one of the poles (which one depends on the sign of the charge of the particle).

4 OUTLINE OF THE MODEL

With this justification of the vacuum assumption for the magnetosphere, the basic model can be defined as a rough approximation to a global self-consistent solution to the pulsar problem. The outer magnetosphere ($r > 0.1R_{\text{lc}}$) is the region of particle acceleration, where charges can be ejected from the magnetosphere. The only radiation which is important is curvature radiation, for the reasons discussed earlier.

Particles radiate gamma-ray photons, some toward the star, where they create electron-positron pairs on the powerful magnetic fields in the inner magnetosphere. These charges are all bound on closed paths to the inner magnetosphere, and cannot populate the outer magnetosphere to short out the large electric fields. A charge balance is established by having charges being created near the star and flowing out with low energies along the null surfaces. The effect of the outflowing charges on the fields is neglected.

Since the paths of the charges are all bound for radii $r < 0.1R_{\text{lc}}$, charges were started on a sphere of radius $0.2R_{\text{lc}}$ (called the “starting sphere”) at intervals of $\pi/16$ radians in the toroidal and poloidal angles to fully sample the range of initial starting positions. The starting energies were unimportant, since the charges immediately move to balance radiation power out with electric field power in. The source for these charges is left undetermined.

The radiation from these trajectories was calculated and binned to build up light curves and spectra for different viewing directions; this is discussed in detail in sections 5 and 7

To simplify the numerical calculation, we took advantage of three symmetries of the problem. First, there is a symmetry (Symmetry 1) in the fields $\vec{E} \rightarrow -\vec{E}$ and $\vec{B} \rightarrow -\vec{B}$ under a translation $\phi \rightarrow \phi + \pi$, $\theta \rightarrow \pi - \theta$, where θ is the poloidal angle and ϕ is the toroidal angle relative to the rotation axis. Therefore, if a charge q started at \vec{r}_0 follows the path $\vec{r}(t)$, the same charge started at $-\vec{r}_0$ will take the path $-\vec{r}(t)$. The symmetry applies for any orientation of the dipole moment to the rotation axis.

The second symmetry (Symmetry 2) is between charges of different sign, but only applies when the dipole axis is

perpendicular to the rotation axis. The path of a charge $-q$ started at (r_0, θ, ϕ) is equal to the path of a charge q started at $(r_0, \theta, \phi + \pi)$ rotated through 180 degrees toroidally.

The third symmetry (Symmetry 3) is a result of another property of the fields, that $\vec{E}(r, \theta, \phi, t)$ equals $\vec{E}(r, \theta, \phi - \Omega t, 0)$ rotated through an angle Ωt in ϕ . This means that a charge q started at (r_0, θ, ϕ, t_0) will follow the path of a charge q started at $(r_0, \theta, \phi - \Omega t_0, 0)$ rotated through Ωt_0 toroidally. This symmetry holds for any orientation of the dipole moment.

Symmetry 1 means than runs need be done only for particle starting points in the top half of the magnetosphere; paths in the bottom half are reflections of those in the top half. A consequence of Symmetry 3 is that charges started at a time t_0 not equal to zero can be found from the paths started at $t_0 = 0$ by a rotation azimuthally. Symmetry 2 means that positron paths can be inferred from electron paths, but only in the orthogonal Deutsch fields.

The combination of Symmetry 2 and Symmetry 3 has an important consequence for the inferred light curves when the dipole moment is perpendicular to the rotation axis: positrons will radiate in exactly the same manner as electrons, but a half period later. If the electron contribution is a single peak, the positrons will contribute a second peak, exactly 0.5 later in phase, if the distribution of positrons is equal to that of electrons in the magnetosphere. This does not hold for non-orthogonal systems, as Symmetry 2 is broken.

5 LIGHT CURVE GENERATION

With paths of all the charges known, a pattern of radiative emission for different retarded times τ ($\tau = t - \hat{n}_{\text{obs}} \cdot \vec{r}/c$, with \hat{n}_{obs} a unit vector pointing toward the observer) could be generated.

A numerical routine stepped along the paths for each of the different starting angles, and for 100 steps in starting angle t_0 . The emission from paths in the bottom half of the magnetosphere (and for positron paths when considering orthogonal fields) was included by inferring their paths from the three symmetries discussed earlier.

Since the emission generated is only for a single electron started at (θ, ϕ) on the starting sphere and at time t_0 , the power must be scaled by a distribution function $f_{e,p}$ of charges over the starting sphere and over starting time, where $f_{e,p} d\Omega dt_0$ is the number of charges (either electrons or positrons) flowing through the starting sphere between solid angle Ω and $\Omega + d\Omega$ at times between t_0 and $t_0 + dt_0$. This distribution function can be varied to model different sources; however, since most emission comes from the outgoing paths, which only originate on a small region of the starting sphere, changes in $f_{e,p}$ do not much affect the light curves. Throughout this work, $f_e = f_p = f$ for the light curve generation; the actual value of f is constrained by the total power emitted by the pulsar, and sets the number density at the starting sphere.

The spectrum of the radiation at one point along a path, for a given particle Lorentz factor and path radius of curvature, is assumed to be instantaneously that for circular motion; this is discussed in section 7 The emitted radiation was cal-

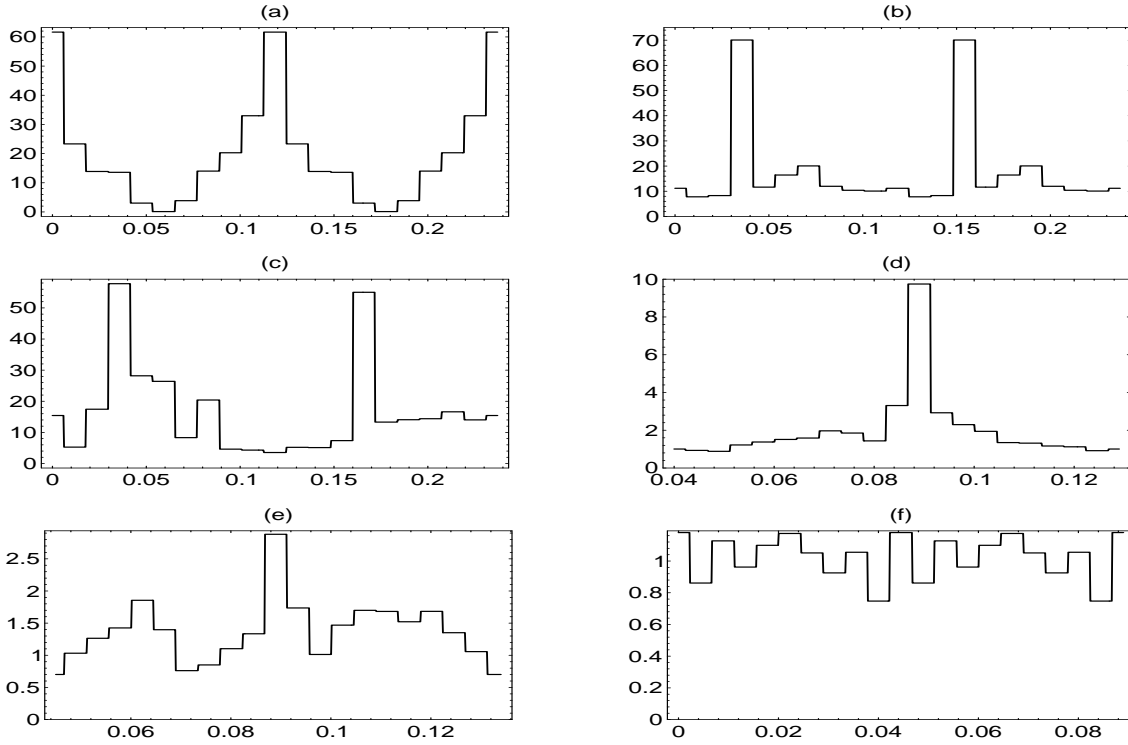


Figure 4. Representative light curves produced by the model for different viewing directions, spin rates, field strengths, and dipole inclinations. See the text for a complete discussion. Time is plotted along the horizontal axis, and arbitrary intensity along the vertical. All plots have radio peaks at $\tau = 0$ and/or $\tau = \pi/\Omega$, presuming the radio emission to be generated close to the star and near the pole. Plot (d) is shown offset in time to show the single peak more clearly.

culated at several different frequencies to capture the spectrum at each time on the light curve.

The emitted power was binned into angular bins of $\pi/16$ radians in azimuthal and poloidal viewing angles, bins of $T/20$ in τ (where T is the pulsar period), and bins of 0.25 in $\log \omega$, where $\hbar\omega$ is the photon energy. Any emission which was beamed through the inner magnetosphere ($r < 0.1R_{\text{lc}}$) was not included in the light curves, as it was assumed to have been absorbed in the denser plasma near the star.

Figure 4 shows some representative 1 MeV light curves generated by the model, which cover many of the variations seen in the observed gamma-ray pulsar light curves. Plots (a) and (b) correspond to a Geminga-like pulsar, with an angular velocity of $\Omega = 26.5$ rad/s and a magnetic dipole moment of $\mu = 10^{30}$ G cm³ aligned perpendicular to the rotation axis. The first is for a viewing angle of $\theta_v = 84.4^\circ$, and the second represents radiation into $\theta_v = 50.6^\circ$. These show the characteristic symmetry between the first and second halves of the light curve due to the action of Symmetry 2 in

the orthogonal field. Light curve (c) is for the same Geminga-like pulsar, but with the dipole moment inclined at 45° to the rotation axis, seen at a viewing angle of 73° . The two main peaks are separated by a phase of 0.45. (d), (e), and (f) all correspond to emission from a Vela-like pulsar, with $\Omega = 70.6$ rad/s and $\mu = 3.7 \times 10^{30}$ G cm³. The dipole moment in (d) and (e) is nearly aligned at only 11.25° to the rotation axis; (f) corresponds to orthogonal fields. (d) represents emission into a viewing angle of 16.9° , and shows a well-defined single peak. (e) is seen from a viewing angle of 61.9° and shows three quite well-defined peaks (there is a suggestion of a triply-peaked light curve for PSR B1706-44 - Thompson et al, 1995). (f) is seen from a viewing angle of 39.4° , and shows no discernable pulsation at frequencies less than 50 GeV. This pulsar would likely be missed in a pulsar survey.

All the plots discussed relate to emission beamed into $\phi_v = 0$; one of the poles points toward the observer at $t = 0$ at this angle. The light curves for $\phi_v \neq 0$ are identical except

for a phase change. For all these plots, the radio emission peaks (presumed to come from the poles near the star) would be seen at $\tau \simeq 0$ and/or $\tau = \pi/\Omega$; the gamma-ray peaks are significantly displaced in some cases, while in others they align quite closely.

6 TOTAL EMITTED POWER

The total power emitted into all directions by the electrons or positrons at any time t is given by:

$$P_{e,p}(t) = \int_{\Omega} \int_{t_0} [f_e \hat{P}_e + f_p \hat{P}_p] d\Omega dt_0 \quad (16)$$

where $\hat{P}_{e,p}(\theta, \phi, t_0; t - t_0)$ is the power output of one electron (e) or positron (p) at time $t - t_0$ along the path, started at (θ, ϕ) on the starting sphere at time t_0 . $f_{e,p}$ are the distribution functions of charges on the starting sphere, which is not fixed in the model.

6.1 The Required Number Density

If the total high-energy power output of a pulsar is known, this fact can be used to estimate the number density of charges at the starting sphere required to supply that energy. If this number density is larger than the Goldreich-Julian number density, the fields will be altered and the model will break down.

Taking a constant distribution $f_e = f_p = f$, the total energy radiated in one period is given by

$$E = f \int_{\Omega} \int_{t_0} \int_t (\hat{P}_e + \hat{P}_p) dt dt_0 d\Omega \quad (17)$$

Since the radiation reaction force fixes the radiated power to be very closely equal to the power input from the electric field,

$$\hat{P}_{e,p} = e \vec{E} \cdot \vec{v}_{e,p} = ec \frac{\mu \Omega^3}{c^3} \vec{E} \cdot \vec{\beta}_{e,p} \quad (18)$$

where \vec{E} is a dimensionless electric field which no longer depends on the values of μ and Ω , and $\vec{\beta}_{e,p} = \vec{v}_{e,p}/c$.

Defining $\tau_0 = \Omega t_0$ and $\tau = \Omega t$, the total energy emitted in a period can now be written

$$E_{\text{tot}} = f \frac{e \Omega \mu}{c^2} \mathcal{E} \quad (19)$$

where \mathcal{E} is a dimensionless function of the dipole inclination angle χ alone:

$$\mathcal{E} = \int_{\Omega} \int_{\tau_0=0}^{2\pi} \int_{\tau=0}^{2\pi} \vec{E} \cdot (\vec{\beta}_e + \vec{\beta}_p) d\Omega d\tau_0 d\tau \quad (20)$$

For example, $\mathcal{E} = 36$ for the orthogonal fields, and 6.8 for $\chi = 11.25^\circ$.

Since the total gamma-ray power output from the model must be constant with time, the total energy emitted in a period is equal to $P_{\text{obs}} \frac{2\pi}{\Omega}$, where P_{obs} is the observed gamma-ray power.

The value of f can then be related to the observed power output:

$$f = \frac{2\pi c^2 P_{\text{obs}}}{e \Omega^2 \mu \mathcal{E}} \quad (21)$$

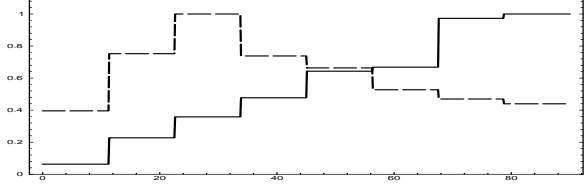


Figure 5. Distribution of emitted power at 1 MeV with viewing angle for two Vela-like pulsars. The solid line shows the power emitted by a pulsar with orthogonal fields, and the dashed line shows the corresponding curve for a pulsar with a dipole axis inclined at 11.25° to the rotation axis. The axes show viewing angle in degrees on the horizontal and emitted power scaled to unity at the maxima on the vertical.

The value of f sets the number density at the starting sphere required to produce the observed power output, since $f = 4\pi c(0.2R_{\text{lc}})^2 n$. Therefore,

$$n = \frac{25 P_{\text{obs}}}{2ec\mu\mathcal{E}} \quad (22)$$

The number density can be described somewhat more meaningfully as a fraction of the Goldreich-Julian number density (equation (3)) at the starting sphere (\mathcal{E} is taken to be equal to 36, the value for the orthogonal fields).

$$\frac{n}{n_{\text{GJ}}} \simeq 4.7 \times 10^{-5} \text{cm}^{-3} \left(\frac{P_{\text{obs}}}{10^{34} \text{ergs/s}} \right) \left(\frac{\Omega}{100 \text{rad/s}} \right)^{-4} \left(\frac{\mu}{10^{30} \text{Gcm}^3} \right)^{-2} \quad (23)$$

This quantity is tabulated in Table 1 for the known gamma-ray pulsars, and is less than unity, and therefore consistent with the model, in all cases. The values of μ were calculated with equation (4) taking $\sin \chi = 1$ (and are therefore a lower limit).

The most serious problem with this model is its inability to *predict* the total power output; instead, it is only shown that the observed power outputs require number densities less than the Goldreich-Julian number density, and therefore are consistent with the assumption of vacuum around the star. The source of the charge on the starting sphere is left unexplained.

6.2 The Gamma-Ray Efficiency

The gamma-ray efficiency of a pulsar is defined as the ratio of the power output in gamma-rays to the total energy loss. For the Deutsch field pulsar, the rate of rotational energy loss is

$$P_{\text{rot}} = \frac{2\Omega^4 \mu^2 \sin^2 \chi}{3c^3} \quad (24)$$

$$\simeq 2.5 \times 10^{-32} \Omega^4 \mu^2 \quad (25)$$

and the gamma-ray power emitted in our model is given by

$$P_{\gamma} = \frac{2\mathcal{E}}{25} ec\mu n \quad (26)$$

Pulsar	P	\dot{P}	μ	P_{tot}	n/n_{GJ}	Reference
Geminga	0.237	11.0	1.63	1.6×10^{34}	5.6×10^{-3}	Mayer-Hasselwander et al 1994
Vela	0.0893	125	3.4	6.3×10^{33}	1.0×10^{-5}	Kanbach et al 1994
Crab	0.0333	421	3.8	10^{36}	2.6×10^{-5}	Ulmer et al 1995
PSR1509-58	0.150	1540	15	6.3×10^{35}	4.2×10^{-4}	Laurent et al 1994
PSR1706-44	0.102	93.0	3.1	6.1×10^{34}	2.1×10^{-4}	Thompson et al 1992
PSR1055-52	0.197	5.8	1.1	9.4×10^{33}	3.5×10^{-3}	Fierro et al 1993
PSRB1951+32	0.0395	5.85	0.49	1.3×10^{34}	4.0×10^{-5}	Ramamanamurthy et al 1995

Table 1. Number densities at the starting sphere required to give the observed power outputs for the known gamma-ray pulsars, as a fraction of the Goldreich-Julian number density. Periods P are given in seconds, period derivatives \dot{P} in 10^{-15} s/s, dipole moments μ in units of 10^{30} G cm³, and gamma-ray power outputs P_{tot} in ergs/s. All known high-energy pulsars have $n/n_{\text{GJ}} \ll 1$.

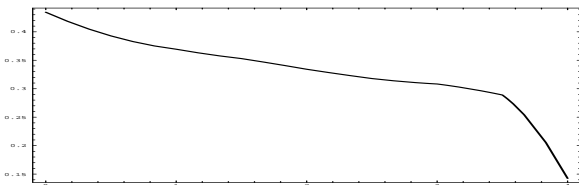


Figure 6. The variation of Ω_p , the fractional solid angle into which radiation is beamed, is shown for a Geminga-like pulsar with a dipole moment inclined at 22.5° to the rotation axis. The pulsar becomes significantly less observable at higher frequencies. Similar results are obtained for pulsars with different model parameters. The axes show the base-10 logarithm of the photon energy in MeV along the horizontal, and the value of Ω_p along the vertical.

Setting $\mathcal{E} = 36$ (orthogonal fields) and writing n in terms of the Goldreich-Julian number density n_{GJ} , the gamma-ray efficiency is

$$\eta_\gamma = \frac{P_\gamma}{P_{\text{rot}} + P_\gamma} \simeq \frac{83 \frac{n}{n_{\text{GJ}}}}{1 + 83 \frac{n}{n_{\text{GJ}}}} \quad (27)$$

Here, the number density has been written as a fraction of the Goldreich-Julian number density; the gamma-ray efficiency only depends on this ratio, not on the pulsar properties directly.

As n/n_{GJ} approaches unity, so does the gamma-ray efficiency. This is seen in the cases of Geminga and PSR1055-52, where the observations suggest that $\eta_\gamma \simeq 1$ (Mayer-Hasselwander et al 1994, Fierro et al 1993).

6.3 The Distribution in Viewing Angle

The emission is not beamed equally into all directions. Figure 5 shows the emission (averaged over a period) at 1 MeV as a function of the viewing angle ($\theta_v = 0$ to 90°) for two Vela-like pulsars: one with orthogonal fields (solid line) and the other with a dipole inclination of 11.25° (dashed line). The power is scaled to unity at the maximum.

The fraction of the total solid angle into which the

power is beamed can be quantified in terms of a power-weighted average:

$$\Omega_p = \int_{\Omega} \frac{P(\Omega)}{P_{\text{max}}} d\Omega \quad (28)$$

where Ω represents solid angle, not the angular velocity of the pulsar.

Figure 6 shows Ω_p as a function of frequency for a Geminga-like pulsar with a dipole moment inclined at 22.5° to the rotation axis. A general trend to lower Ω_p (and therefore less observable pulsars) is seen for increasing frequency, with a much faster dropoff above the break in the spectrum (near several hundred MeV). Similar results are obtained for pulsars with different model parameters.

7 SPECTRA OF EMITTED RADIATION

Since curvature radiation is the only contribution to the light curves, the frequency distribution of curvature emission by a single particle moving instantaneously in circular motion must be considered (see, for example, Jackson (1975)). The shape of the curve depends on only two parameters - the energy of maximum intensity ($E_m = 0.14\hbar\gamma^3 c/\rho$, where γ is the charge's Lorentz factor, c is the speed of light, and ρ is the radius of curvature of the particle's path), and the maximum intensity. For energies much less than E_m , the number distribution in frequency is proportional to $E^{-2/3}$; above E_m , the curve drops off exponentially, and essentially disappears for $E > 30E_m$. This function is plotted in Figure 7.

At low frequencies, therefore, each part of the light curve will fall off in photon number like $E^{-2/3}$, and the shape of the light curve will remain essentially constant. At higher frequencies, the contributions from particles radiating with different E_m 's will result in a light curve which is variable with frequency. If several different locations in the magnetosphere make significant contributions to the power, the shape of the spectrum can deviate significantly from the single-particle spectrum.

Figure 8 shows several different time-averaged spectra from model pulsars, all with $\mu = 10^{31}$ G cm³, $\chi = 90^\circ$, and seen from a viewing angle of 83.4° . Spectra for pulsars with three different angular velocities are shown: $\Omega = 25$ rad/s, 75 rad/s, and 150 rad/s. The slow pulsar shows a very hard spectrum with an energy break near several GeV, but relatively featureless otherwise. The 75 rad/s pulsar shows a slight softening of the spectrum near a few hundred MeV,

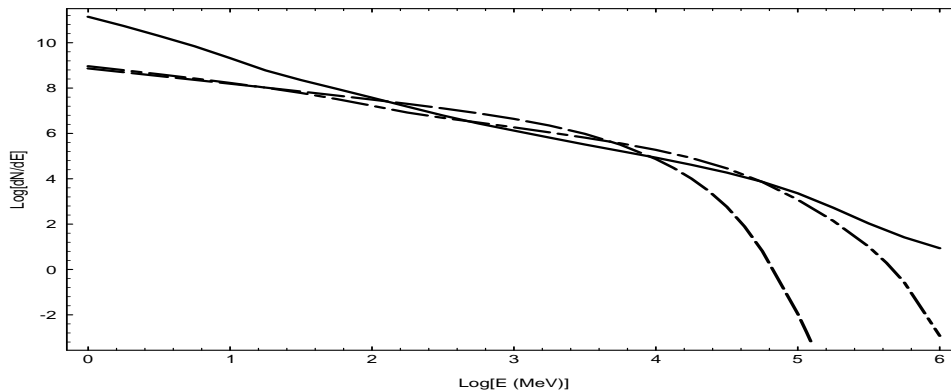


Figure 8. Representative spectra for three model pulsars, all with $\mu = 10^{31}$ G cm³, $\chi = 90^\circ$, and seen from a viewing angle of 84.3° . The solid line corresponds to a pulsar with $\Omega = 150$ rad/s, the dashed-dotted line to one with $\Omega = 75$ rad/s, and the dashed line to $\Omega = 25$ rad/s. The faster pulsars show more spectral detail at low frequency.

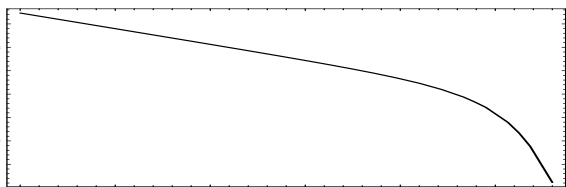


Figure 7. The curvature spectrum for a single particle in instantaneously circular motion. Logarithm of photon energy in units of the reference energy $\hbar\gamma^3 c/\rho$ is shown along the horizontal, and logarithm of arbitrary differential photon number is plotted along the vertical.

and then returning to a hard profile until an energy break near 100 GeV. The 150 rad/s pulsar has a significantly harder spectrum with no break even through the TeV region. It is interesting to note that the photon flux for all three pulsars is relatively constant in the 100 MeV range even though the total power outputs vary considerably.

Figure 9 shows time-averaged spectra for an orthogonal field, Geminga-like pulsar with a dipole moment of 10^{30} G cm³ at a viewing direction of $\theta_v = 84.4^\circ$. The spectrum does change slightly with viewing angle, though the ma-

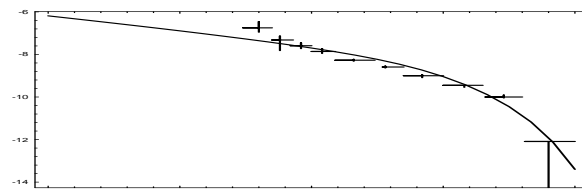


Figure 9. The model spectrum of a Geminga-like pulsar from 1 MeV to 10 GeV. The data shown are EGRET data in the range 40 MeV to 6.3 GeV, from Mayer-Hasselwander et al 1994. The theoretical curve has been shifted vertically on the plot to best fit the data. The horizontal axis shows the logarithm of the energy in MeV, and the vertical axis shows the logarithm of differential photon number in units of photons/s/cm²/MeV.

ior features (location of the energy break and the shape of the spectrum) are roughly the same. Data from Mayer-Hasselwander et al 1994 are shown in the interval 40 MeV to 6.3 GeV; the theoretical curve has been shifted vertically on the plot to best fit the data.

The different regions of the light curve can have somewhat different spectral properties. Figure 10 shows the light curve (c) from Figure 4 separated into four components. The

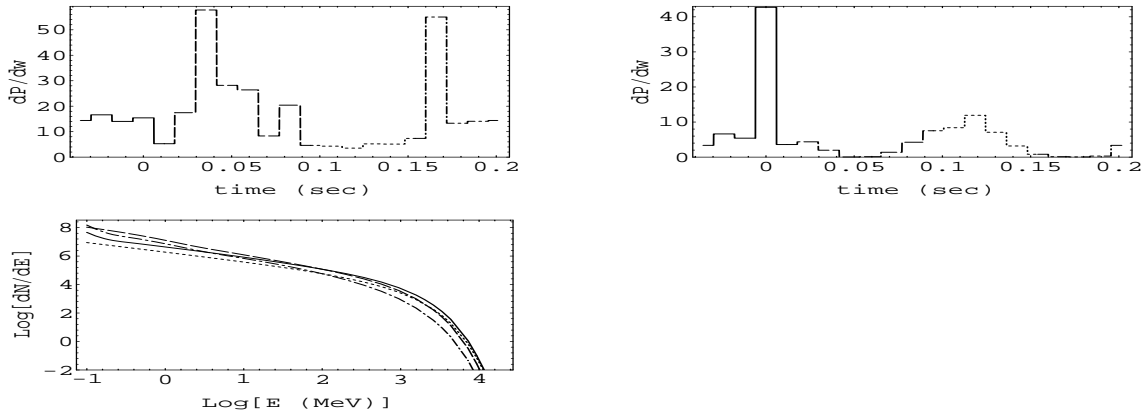


Figure 10. The frequency dependence of the light curve (c) from Figure 4. (a) shows the light curve at 1 MeV, and (b) shows the emission at 10 GeV. (c) shows the spectra for four different components in the light curve. The line dashing of the components in the light curves corresponds to that of the lines in the spectral plot. The axes show the base-10 logarithm of energy in MeV along the horizontal and logarithm of arbitrary differential photon number along the vertical.

components correspond roughly to the peaks at low energy (1 MeV), shown in (a), and the high-energy (10 GeV) peaks, which fall at phases of zero and 0.5.

The phase of the gamma-ray peak tends to change with energy when the energies are close to the energy break if it is significantly different from the phase of the radio peak. This occurs because the emission of highest frequency comes from particles moving nearest to the star, where the fields are larger. As the energy increases past the break, the peaks tend to move into phase with the radio peaks, since both are coming from relatively close to the star near the poles. This alignment of gamma-ray phase with radio phase at high frequencies is a provable prediction of the model, given the presumed location of radio emission. It is difficult to see this effect in the present observations, since the phase change only happens at very high frequencies (typically above 10 GeV). However, if the low-energy gamma peaks are not aligned with the radio peaks, it does lead to the “interpulse” regions at low energy having harder spectra and higher energy breaks than the low-energy pulses, as is seen, for example, in the case of the Vela pulsar (Kanbach et al 1994).

Generally the low-energy spectral index of $-2/3$ is harder than observed in the X-ray region for those pulsars

where this has been measured. However, this is precisely the region where the model begins to break down, and radiation from other areas (such as the inner magnetosphere, where unperturbed curvature radiation likely is not the dominant contribution to the spectrum) becomes important.

8 DISCUSSION

A new model of high-energy pulsar emission has been presented, with the simplifying assumption that the charge densities and current densities are small enough that the electromagnetic fields can be represented by the Deutsch fields in the outer magnetosphere.

The assumption that the magnetosphere can remain evacuated is justified by recognising that charges created near the star follow paths bound to the inner magnetosphere, and cannot short out the fields farther out. We create an approximate self-consistent global solution to the electromagnetic fields and charge motions by extending the “stellar” radius (inside which the fields are frozen-in) to 0.1 of the light cylinder radius; charge created in the inner magnetosphere can flow out along null surfaces where the electric

field is perpendicular to the magnetic field. The outer magnetosphere is the location of particle acceleration and high-energy emission.

An important approximation has been developed to chart particle motion in fields where the timescale required to adjust to the field direction is much less than the timescale to radiate away the charge's momentum perpendicular to the magnetic field, called the drift frame bead-on-a-wire (DFB) approximation. This reduces the problem of particle motion to a simple first order, ordinary set of differential equations, reducing computation time enormously. This approximation could prove useful for developing global, self-consistent models of the pulsar magnetosphere, as it gives a relatively simple description of charge paths in terms of the electric and magnetic fields.

Several constraints on the applicability of the model can be made, the most important of which is that the number density required to produce the observed power output must be much less than the Goldreich-Julian charge density. All observed gamma-ray pulsars satisfy this constraint, as well as that which maintains the dominance of curvature radiation to the high-energy spectrum in the model framework and that which maintains the applicability of the DFB approximation.

The light curves generated from the model match the general properties of the observed light curves quite well. When the magnetic dipole moment is orthogonal to the rotation axis, the light curves are mainly double-peaked; the second half of the light curve is identical to the first. Other inclinations can give single peaks, non-symmetric double peaks, and triple peaks, as well as practically unpulsed emission in some cases.

The biggest weakness of the model is its present inability to predict the actual power output of the pulsars in gamma-rays: it does not assume any value for the number density at the starting sphere, only that it be much less than the Goldreich-Julian number density so that the electric fields are not shorted out. It also says nothing about any radiation produced in the inner, bound magnetosphere, where particle energies will be somewhat lower than those in the outer, evacuated magnetosphere. This might provide significant emission at lower energies.

Our model compares quite favourably with the other popular models for pulsar gamma-ray emission. The spectra predicted by our model match the observations in some cases better than those generated by the outer gap model of Chiang & Romani (1994), and as well as those presented for the extended polar cap model of Daugherty & Harding (1995). Our model also has the potential to generate more complex light curves than either the outer gap or polar cap models, which can only produce single or double peaks. However, this is something of a double-edged sword, as a random sample of light curves would be somewhat less regular than is observed.

This work has introduced the general Deutsch field gamma-ray pulsar model; applications of the model to the known gamma-ray pulsars are developed in Paper II, which also considers several statistical properties of a population of these pulsars.

REFERENCES

- Cheng, K.S., Ho, C., Ruderman, M., 1986, *ApJ*, 300, 500.
 Chiang, J., Romani, R.W., 1994, *ApJ*, 436, 754.
 Daugherty, J.K., Harding, A.K., 1991, *ApJ*, 374, 687.
 Daugherty, J.K., Harding, A.K., 1994, *ApJ*, 429, 325.
 Daugherty, J.K., Harding, A.K., 1995, in preparation (*astro-ph/9508155* in the e-print archives).
 Fierro, J.M., et al, 1993, *ApJ*, 413, L27.
 Grenier, I.A., Hermsen, W., Henriksen, R.N., 1993, *A&A*, 269, 209.
 Higgins, M.G., Henriksen, R.N., 1996, in preparation (Paper II).
 Jackson, J.D., 1975, "Classical Electrodynamics", John Wiley & Sons.
 Kanbach, G., et al, 1994, *A&A*, 289, 855.
 Laurent, P.J., et al, 1994, *A&A*, 286, 838.
 Masnou, J.L., et al, 1994, *A&A*, 290, 503.
 Mayer-Hasselwander, H.A., et al, 1994, *ApJ*, 421, 276.
 Ostriker, J.P., Gunn, J.E., 1969, *ApJ*, 157, 1395.
 Ramanamurthy, P.V., et al, 1995, *ApJ*, 447, L109.
 Thompson, D.J., et al, 1992, *Nature*, 359, 615.
 Thompson, D.J., et al, 1994, *ApJ*, 436, 229.
 Thompson, D.J., et al, 1995, in preparation.
 Ulmer, M.P., et al, 1995, *ApJ*, 448, 356.